PHYSICAL REVIEW B **87**, 195141 (2013)

Multiplet effects in orbital and spin ordering phenomena: A hybridization-expansion quantum impurity solver study

Andreas Flesch and Evgeny Gorelov
Institute for Advanced Simulation, Forschungszentrum Jülich, 52425 Jülich, Germany

Erik Koch
German Research School for Simulation Science, 52425 Jülich, Germany and
JARA High-Performance Computing, RWTH Aachen University, 52062 Aachen, Germany

Eva Pavarini
Institute for Advanced Simulation, Forschungszentrum Jülich, 52425 Jülich, Germany and
JARA High-Performance Computing, RWTH Aachen University, 52062 Aachen, Germany

(Received 20 February 2013; revised manuscript received 3 May 2013; published 30 May 2013)

We use an efficient general hybridization-expansion continuous-time quantum Monte Carlo impurity solver (Krylov approach) to study orbital and spin ordering phenomena in strongly correlated systems within the local-density approximation plus dynamical mean-field theory approach. This allows us to include often-neglected interaction terms, to study models with large basis sets, to consider crystals with low-symmetry distortions, and to reach the very low experimental temperatures. We use this solver to study ordering phenomena in a selection of exemplary low-symmetry transition-metal oxides. For the rare-earth manganites, we show that including spin-flip and pair-hopping terms does not affect the Kugel-Khomskii orbital-order melting transition. For $LaMnO_3$, we find that the commonly used two-band model with classical t_{2g} spin gives a good description of the e_g electrons when compared with the full five-orbital Hubbard model. Surprisingly not only the occupied orbital but also the e_g spectral matrix is well reproduced. For the d^1 perovskites $CaVO_3$ and $YTiO_3$ we show that spin-flip and pair-hopping terms only weakly affect orbital fluctuations. Moreover, for the Mott insulator $YTiO_3$ we can study the ferromagnetic polarization to very low temperatures, finding a transition temperature in remarkably good agreement with experiments.

DOI: 10.1103/PhysRevB.87.195141 PACS number(s): 71.10.Fd, 71.27.+a, 71.28.+d

I. INTRODUCTION

Orbital and magnetic ordering phenomena play a crucial role in the physics of strongly correlated transition-metal oxides. Their onset depends on symmetry, lattice distortions, superexchange interaction, and the form of the Coulomb tensor. The realistic description of ordering phenomena requires the ability to disentangle the effects of all these interactions. In recent years, the local-density approximation plus dynamical mean-field theory (LDA + DMFT) approach,[1–3] which combines *ab initio* techniques based on density functional theory in the LDA and DMFT,[4] has led to important progress in understanding such ordering phenomena. It has been shown that many-body superexchange only weakly affects the onset of the orbital-order-to-disorder transition in rare-earth manganites,[5] whereas, in the presence of strong Coulomb repulsion, a small crystal field is sufficient to strongly suppress orbital fluctuations and stabilize orbital order.[5–7] However, the effects of subtle Coulomb interactions, such as spin-flip and pair-hopping terms, or of quantum fluctuations, e.g., charge fluctuations between half-filled t_{2g} and e_g states in manganites or spin fluctuations, are not yet fully understood, while the origin of very low-temperature magnetism in multiorbital materials remains little investigated in a realistic context. The hybridization-expansion continuous-time quantum Monte Carlo (CT-HYB) technique[8–13] appears to date the most promising DMFT quantum impurity solver to study real materials at experimental temperatures, although most calculations so far have been limited to high-symmetry cases or systems for which the hybridization function is diagonal (or almost diagonal) in orbital space.[8–11,14]

In the present work we study the effects of commonly adopted approximations on the origin of orbital and magnetic order in some exemplary low-symmetry transition-metal oxides. To do this, we use an efficient general implementation of the CT-HYB quantum Monte Carlo (QMC) LDA + DMFT solver for systems of arbitrary point symmetry and arbitrary local Coulomb interaction. In our implementation we combine a general Krylov[11] scheme, which we use for the low-symmetry cases, with a very fast segment implementation,[8] which can be used when the local Hamiltonian does not mix flavors (i.e., spin-orbital degrees of freedom). In addition, we use symmetries[10,12] to minimize the computational time. We present results for the orbital melting transition in the rare-earth manganites $RMnO_3$, orbital fluctuations in the $3d^1$ perovskites $CaVO_3$ and $YTiO_3$, and ferromagnetism in the Mott insulator $YTiO_3$. Finally, we investigate the regime of validity of the t_{2g} classical spin approximation often adopted to describe $LaMnO_3$ and more general manganites.

The paper is organized as follows. In Sec. II we briefly discuss the approach in the context of the LDA + DMFT method. Sections III and IV give our results. In Sec. III we present applications to rare-earth manganites. We show that spin-flip and pair-hopping terms do not affect the Kugel-Khomskii orbital-order transition. For $LaMnO_3$ we show that the e_g two-band Hubbard model, commonly used to study the system, in which the t_{2g} electrons are treated as disordered

classical spins interacting with the e_g spins via the Coulomb interaction, yields results in very good agreement with the full five-orbital $3d$ Hubbard model. Remarkably, the agreement between the two models is not only excellent for the occupied state in the orbitally ordered phase, but also very good for the orbital-resolved e_g spectral function matrix. In Sec. IV we consider vanadates and titanates. We calculate orbital fluctuations in $CaVO_3$ and $YTiO_3$ and find that the effect of spin-flip and pair-hopping terms is weak. Moreover, we calculate the ferromagnetic transition temperature for the Mott insulator $YTiO_3$ and find excellent agreement with experiments, showing that orbital order is indeed compatible with ferromagnetism in this material, contrary to an early hypothesis.[15] Section V gives our conclusions. In the Appendix we describe the details of our implementation of the general CT-HYB solver.

II. MODEL AND METHOD

The most general multiband Hubbard model for transition-metal oxides is given by

$$H = -\sum_{i\neq i'}\sum_{\sigma,\sigma'}\sum_{m,m'} t^{ii'}_{m\sigma m'\sigma'} c^{\dagger}_{im\sigma} c_{i'm'\sigma'} + \sum_{i}\sum_{\sigma,\sigma'}\sum_{m,m'} \varepsilon_{m\sigma m'\sigma'} c^{\dagger}_{im\sigma} c_{im'\sigma'} + \frac{1}{2}\sum_{i}\sum_{\sigma,\sigma'}\sum_{mm'\tilde{m}\tilde{m}'} U_{mm'\tilde{m}\tilde{m}'} c^{\dagger}_{im\sigma} c^{\dagger}_{im'\sigma'} c_{i\tilde{m}'\sigma'} c_{i\tilde{m}\sigma}. \quad (1)$$

Here $c^{\dagger}_{im\sigma}$ ($c_{im\sigma}$) creates (annihilates) an electron with spin σ in orbital m on lattice site i; $t^{ii'}_{m\sigma m'\sigma'}$ are the hopping integrals and $\varepsilon_{m\sigma m'\sigma'}$ the elements of the crystal-field matrix obtained from LDA calculations by constructing a localized Wannier-function basis.[6,16] $U_{mm'\tilde{m}\tilde{m}'}$ are the screened Coulomb matrix elements, typically expressed in terms of the three Slater integrals F_0, F_2, and F_4, with $U_{\rm av} = F_0$ (direct Coulomb interaction) and $J_{\rm av} = \frac{1}{14}(F_2 + F_4)$ (exchange Coulomb interaction). In the following we find it more useful to use as parameters[3,17] the diagonal element of the Coulomb matrix, $U_0 = F_0 + \frac{8}{5}\tilde{J}$, the Kanamori exchange parameter $\tilde{J} = \frac{5}{7}J_{\rm av}$, and the Coulomb anisotropy $\delta\tilde{J} = \tilde{J}(\frac{1}{5} - \frac{1}{9}\frac{F_4}{F_2})/(1 + \frac{F_4}{F_2})$. The exchange couplings for e_g and t_{2g} only are then $J_{e_g} = \tilde{J} + 3\delta\tilde{J}$ and $J_{t_{2g}} = \tilde{J} + \delta\tilde{J}$. We solve the model (1) with DMFT using the CT-HYB QMC approach as a quantum impurity solver.[8–10] Our implementation of the CT-HYB QMC solver is discussed in the Appendix. It works efficiently for systems of arbitrary space-group symmetry, i.e., with both a hybridization-function matrix and self-energy matrix in the full spin-orbital space. We optimize our code for modern massively parallel architectures and exploit symmetries to minimize the computational time. We use two approaches to calculate the trace which enters in the numerical evaluation of the Green's function: the segment approach[8] and the Krylov method.[11] The segment approach is very fast but can only be used if the local Hamiltonian does not mix flavors (spin-orbital degrees of freedom). The Krylov procedure is instead general and scales linearly with the inverse temperature, becoming therefore particularly efficient in the low-temperature regime.[12,13] Far from phase transitions, we further enhance the efficiency by adaptively truncating the local trace in the Green's function.[11,12] Further details on our code are given in the Appendix. This efficient implementation allows us to include in the model Hamiltonian (1) typically neglected interactions, such as spin-flip and pair-hopping terms or spin-orbit coupling, to study models with larger number of orbitals (e.g., with the complete five-orbital d shell), and reach very low temperatures, essential to study magnetic transitions. In the following, we use our code to systematically compare different models and test typically adopted approximations on the orbital and magnetic order of a selection of exemplary materials.

III. ORBITAL-ORDER MELTING IN RARE-EARTH MANGANITES

The origin of the orbital-order melting transition[18] in the rare-earth manganites $R\mathrm{MnO_3}$ with the $t^3_{2g}e^1_g$ nominal electronic configuration has long been debated. Recently,[5,19] we have shown that for $LaMnO_3$ superexchange alone yields a large orbital transition temperature $T_{\rm KK} \sim 600$ K. This value is very close to the experimental orbital-order melting temperature $T_{\rm JT} \sim 750$ K. It was already suggested early on that superexchange effects in $LaMnO_3$ could be so large.[20] However, our calculations show in addition that in the $R\mathrm{MnO_3}$ series $T_{\rm KK}$ slightly decreases with decreasing ionic radius, while the experimental $T_{\rm JT}$ dramatically increases. This indicates that the many-body superexchange interaction plays a small role in determining the orbital-order melting temperature $T_{\rm JT}$ and the trend of $T_{\rm JT}$ with decreasing radius of the rare-earth ions. However, spin-flip and pair-hopping terms, neglected in previous calculations, restore the full degeneracy[21–23] of the e_g multiplets and could enhance the strength of superexchange or even modify the occupied orbital.[24] Furthermore, previous calculations, like most many-body studies of rare-earth manganites, rely on the classical spins approximation for t_{2g} orbitals.[25] In this approximation the effects of the t_{2g} spins ($S_{t_{2g}} = 3/2$) on the e_g states is described through a local magnetic field due to the e_g-t_{2g} Coulomb exchange interaction and a bandwidth renormalization factor arising from the spatial disorder in the orientation of the t_{2g} spins. However, charge fluctuations between t_{2g} and e_g states or t_{2g} multiplet fluctuations, not accounted for in such a model, could affect the orbital order and the occupied orbital. In this section we use our implementation of the CT-HYB QMC solver to analyze these effects.

A. Role of spin-flip and pair-hopping interactions

First we analyze the role of spin-flip and pair-hopping interactions in the orbital melting transition. The minimal Hubbard Hamiltonian which is believed to retain the essential physics[25] to study this issue is a two-band Hubbard model for e_g states coupled to disordered t_{2g} spins via the Coulomb interaction, which acts as a local magnetic field $h = J_{t_{2g}} S_{t_{2g}}$. Thus, in Hamiltonian (1) the one-electron term becomes

$$\varepsilon_{m\sigma m'\sigma'} = \left(\varepsilon_{\rm JT}\tau^i_x + \varepsilon_{\rm T}\tau^i_z\right)\delta_{\sigma,\sigma'} - h\sigma^i_z,$$
$$t^{ii'}_{m\sigma m'\sigma'} = u_{\sigma,\sigma'} t^{ii'}_{mm'}.$$

The index m runs over the e_g Wannier orbitals $|x^2 - y^2\rangle$ and $|3z^2 - r^2\rangle$, σ_z is the Pauli z matrix, and τ_x and τ_z are pseudospin operators acting on orbital degrees of freedom ($\tau_z|3z^2 - r^2\rangle = 1/2|3z^2 - r^2\rangle$, $\tau_z|x^2 - y^2\rangle = -1/2|x^2 - y^2\rangle$, $\tau_x|3z^2 - r^2\rangle = |x^2 - y^2\rangle$). The energies $\varepsilon_{\rm JT}$ and $\varepsilon_{\rm T}$ yield, respectively, the Jahn-Teller and tetragonal crystal-field splitting. Finally $u_{\sigma,\sigma'} = 2/3$ is a band renormalization factor which accounts for the disorder in the orientations of the t_{2g} spins.[25] For the effective magnetic field h, we present calculations for the theoretical estimate[26] $h \sim 1.35$ eV; our results for the orbital-melting transition and the orbital polarization are, however, weakly dependent on h in the relevant regime, in which e_g and t_{2g} spins are locally aligned. For the e_g basis, the Coulomb interaction is composed of density-density interactions, and spin-flip and pair-hopping terms. We use the theoretical estimates $U_0 = 5$ eV and $J_{e_g} \sim \tilde{J} \sim 0.76$ eV for the e_g screened direct and exchange on-site Coulomb interaction.[5,26,27] In order to calculate the critical temperature due to superexchange only, we set the crystal-field parameters to zero: $\varepsilon_{\rm JT} = \varepsilon_{\rm T} = 0$. This disentanglement procedure was proposed in Ref. 7 and was successfully used to study orbital order in cuprates and manganites.[5,7,19] The transition can be determined either from the orbital polarization as determined from the occupations[7] of the natural orbitals (order parameter) or from the energy gain due to orbital polarization.[19] The two approaches give very similar results.[19] Here we use the first.

We show in Fig. 1 the results of our calculations based on our CT-HYB QMC solver; we use the Krylov approach for the model with spin-flip and pair-hopping terms and the segment method for the model with density-density Coulomb terms only. The figure shows the orbital-order transition temperature due to superexchange only, $T_{\rm KK}$, for relevant elements of the series of rare-earth manganites. It demonstrates that the spin-flip and pair-hopping terms affect very little the overall trends and even the absolute value of $T_{\rm KK}$. These results all reinforce previous conclusions[19] that superexchange has a small influence in determining the orbital-order-to-disorder transition observed in rare-earth manganites.

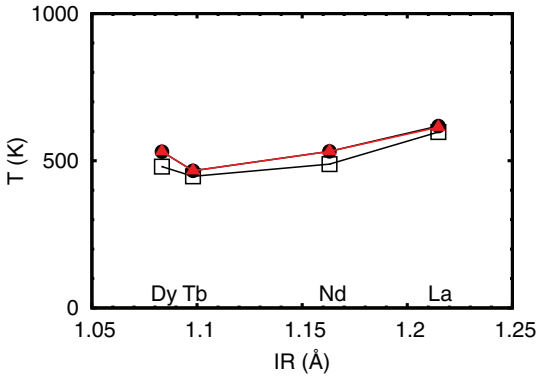

FIG. 1. (Color online) Orbital-order transition temperature due to superexchange, $T_{\rm KK}$, versus the R^{3+} ionic radius in the RMnO$_3$ series (R = Dy, Tb, Nd, La). Open squares: $T_{\rm KK}$ taken from Ref. 19; calculations were done for density-density Coulomb interactions and using a Hirsch-Fye QMC solver. Light triangles: CT-QMC (segment solver) and density-density Coulomb interactions only. Black circles: CT-QMC (Krylov solver) and full Coulomb interaction.

B. Classical t_{2g} spins versus full five-band model for LaMnO$_3$

Next we test the validity of the classical t_{2g} spin approximation for the orbital-order melting transition. To do this, we compare the results of the previous section with those obtained for the full five-band Hubbard model described by Hamiltonian (1). To study the orbital order due to superexchange only, we again set to zero the crystal-field splitting within the e_g doublet and t_{2g} triplet; however, we retain the cubic crystal field which splits t_{2g} and e_g. Finally, we perform the LDA + DMFT calculations at $T \sim 290$ K, i.e., well below $T_{\rm KK}$. Since we have already shown that spin flip and pair hopping do not affect the transition temperature, we neglect them here to speed up the calculations. Furthermore, to compare directly the results of the two- and five-band models, we assume $J_{e_g\text{-}t_{2g}} \sim h/S_{t_{2g}}$ for the e_g-t_{2g} exchange coupling and neglect other small Coulomb anisotropies. The LDA + DMFT calculation for the five-band model yields half-filled t_{2g} states and almost fully polarized e_g states. The occupied e_g state $|\theta\rangle = \cos\frac{\theta}{2}|3z^2 - r^2\rangle - \sin\frac{\theta}{2}|x^2 - y^2\rangle$ is the orbital with $\theta \sim 90^o$, in excellent agreement with the results from the classical t_{2g} spins approximation, which gives basically the same state. The spectral function matrices calculated for the five- and two-band models are compared in Fig. 2. This figure shows that not only the orbitals but also, surprisingly, the overall spectral function matrices from the two models are in good agreement. Because the five-band

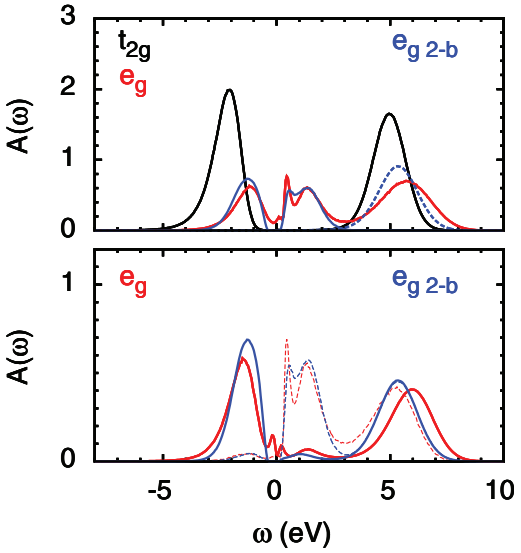

FIG. 2. (Color online) Top: LaMnO$_3$, comparison of the spectral function matrix obtained for the five-band Hubbard model and the e_g two-band model with classical t_{2g} spins. Calculations have been performed at $T \sim 290$ K and $U_0 \sim 5$ eV. The chemical potential μ is at energy zero for the two-band model and at ~0.3 eV for the five-band model. The Jahn-Teller and tetragonal crystal-field splittings are set to zero. Black line, t_{2g} spectral function; light lines, e_g spectral function from the five-band model; dark lines, e_g spectral function from the two-band model, spin up (solid line) and down (dashed line). The position of the spin-down Hubbard band depends on the effective magnetic field h, i.e., on $J_{t_{2g}}$. Bottom: Comparison of the e_g spectral function matrices, orbitally resolved. Solid (dashed) lines: most (least) occupied orbital. Dark (light) lines: two-band (five-band) model.

model includes the full dynamics of the t_{2g} electrons,[21] the effective U_0 is larger than for the two-band model. By scanning different U_0 between 7 and 5 eV we find that $U_0 \sim 5.5$ eV yields a gap quite close to that of the two-band model and a spectrum in good agreement with experiments. This shows that in the two-band model the Coulomb integral U_0 is screened $\sim$10% by the t_{2g} electrons. The half-filled t_{2g} bands exhibit a very large gap because at half filling the t_{2g} exchange couplings effectively enhance the effect of the Coulomb repulsion U_0. Finally, we find the on-site spin-spin correlation function to be $\langle S_z^{t_g} S_z^{e_g} \rangle \sim 0.74$, very close to the value of 0.75 expected for aligned e_g and $S_{t_{2g}} = 3/2$ t_{2g} spins. Concerning the sign problem, we find it negligible for all of these calculations (the average sign is $\sim$0.99 in the worst case).

IV. ORBITAL FLUCTUATIONS AND MAGNETISM IN $CaVO_3$ AND $YTiO_3$

The importance of orbital fluctuations in the physics of $3d^1$ perovskites has long been debated.[6,15,16,28–30] Single-site DMFT calculations have shown that in the presence of crystal-field splitting Coulomb repulsion strongly suppresses orbital fluctuations.[6] However, these conclusions were based on a Hubbard model with density-density Coulomb interactions only. In this section we analyze the effect of the neglected spin-flip and pair-hopping Coulomb interactions. Furthermore, exploiting our efficient CT-HYB solver, we address the issue of the nature of the low-temperature (30 K)[15,31] ferromagnetic transition in $YTiO_3$.

A. Orbital fluctuations

The minimal model to consider for $3d^1$ transition-metal oxides is a three-band Hubbard model for the t_{2g} bands including spin-flip and pair-hopping terms, and with

$$\varepsilon_{m\sigma m'\sigma'} = \varepsilon_{mm'}\delta_{\sigma,\sigma'},$$
$$t^{ii'}_{m\sigma m'\sigma'} = t^{ii'}_{mm'}\delta_{\sigma,\sigma'},$$

where $m,m' = xy,xz,yz$. For the Coulomb parameters we use $U_0 = 5$ eV and $J_{t_{2g}} \sim 0.68$ eV ($CaVO_3$) or $J_{t_{2g}} = 0.64$ eV ($YTiO_3$) from theoretical estimates and previous works.[6,27] Because the local Hamiltonian mixes flavors even in the crystal-field basis, i.e., the basis diagonalizing the *noninteracting* part of the local Hamiltonian, we perform the LDA + DMFT calculations using the Krylov version of our general CT-HYB QMC solver.

In Table I we show the occupations n_i of the natural orbitals, i.e., the eigenstates of the one-body density matrix, at $\sim$190 K in $CaVO_3$ and $YTiO_3$. We find that $CaVO_3$ is a paramagnetic metal with a small orbital polarization. Instead, $YTiO_3$ is a paramagnetic insulator with orbital polarization $p = n_1 - (n_2 + n_3)/2 \sim 1$, i.e., basically full (orbitally ordered state). For this system, the double occupancies at 290 K are small; i.e., we find $\frac{1}{2}\sum_{m\sigma\neq m'\sigma'}\langle \hat{n}_{m\sigma}\hat{n}_{m'\sigma'}\rangle \sim 0.015$ for $YTiO_3$. The occupied orbital is $|1\rangle = 0.611|xy\rangle - 0.056|xz\rangle + 0.789|yz\rangle$. We find the occupied state and orbital polarization are basically the same with full Coulomb and density-density approximations. Previous calculations[6] in which spin-flip and pair-hopping terms have been neglected and $T \sim 770$ K are in line with these results. This shows that spin-flip and pair-hopping terms do not change the conclusion that orbital fluctuations are strongly suppressed in the Mott insulator $YTiO_3$. In the CT-HYB QMC simulations the average sign is $\sim$0.9 for $YTiO_3$ and $\sim$0.95 for $CaVO_3$.

TABLE I. Occupations n_i of the natural orbitals (with $n_i > n_{i+1}$) at $T = 190$ K in $CaVO_3$ and $YTiO_3$ obtained by diagonalizing the occupation matrix. For $YTiO_3$ the occupied orbital is the natural orbital $|1\rangle = 0.611|xy\rangle - 0.056|xz\rangle + 0.789|yz\rangle$, and it basically coincides with the lowest-energy crystal-field state; we find about the same occupied orbital by performing the calculation with and without pair-hopping and spin-flip terms, or in the paramagnetic and in the ferromagnetic phase.

	n_1	n_2	n_3
$CaVO_3$	0.47	0.28	0.25
$YTiO_3$	0.98	0.01	0.01

B. Ferromagnetism in $YTiO_3$

$YTiO_3$ is one of the few ferromagnetic Mott insulators. Neutron scattering experiments pointed out early-on the difficulties in reconciling ferromagnetism and the expected orbital order,[15] and there have been suggestions that the ferromagnetic state could rather be associated with a quadrupolar order and large-scale orbital fluctuations.[29] However, second-order perturbation theory calculations indicate that ferromagnetism and orbital order could be reconciled, provided that the real crystal structure of $YTiO_3$, including the $GdFeO_3$-type distortion (tilting and rotation of the octahedra, and deformation of the cation cage), is taken into account.[16] To clarify this point, we check the instability towards ferromagnetism of the three-band t_{2g} Hubbard model obtained for the experimental structure of $YTiO_3$. With this approach we calculate the ferromagnetic transition temperature T_C due to superexchange alone in the orbitally ordered phase. Since experimentally $T_C \sim 30$ K, we have to perform LDA + DMFT calculations down to very low temperatures, which becomes possible with the CT-HYB QMC solver. On lowering the temperature, we find that the sign problem becomes sizable (average sign $\sim$0.7 at 40 K). However, we can basically eliminate it (average sign $\sim$0.97) by performing the LDA + DMFT calculations

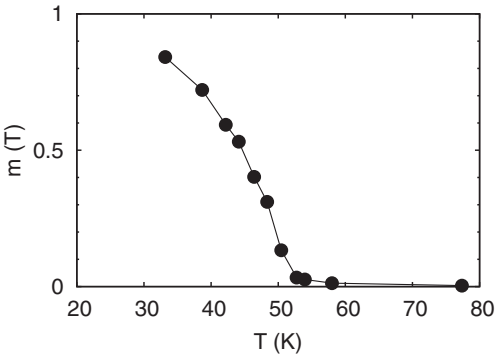

FIG. 3. Ferromagnetic spin polarization as a function of temperature in $YTiO_3$. The plot shows a transition at the critical temperature $T_C \sim 50$ K, slightly overestimating the experimental value $T_C \sim 30$ K, as one might expect from a mean-field calculations.

in the basis which diagonalize the crystal-field matrix, even though the hybridization function has off-diagonal terms of comparable size in the two bases. In Fig. 3 we show the LDA + DMFT magnetization $m(T)$ of the t_{2g} states as a function of the temperature. Remarkably, we find a transition at about 50 K, in excellent agreement with experiments,[32] which yields $T_C \sim 30$ K; the overestimation can be ascribed to the mean-field approximation and to the fact that, since the critical temperature is very small, it is sensitive to tiny details, in particular the exact value of the screened exchange integral J. The occupied orbital does not change significantly in the magnetic phase, indicating that the occupied orbital remains the one that diagonalizes the crystal-field matrix; i.e., in the magnetic phase there is no sizable change of orbital[5,19] due to superexchange.

V. CONCLUSIONS

We have implemented an efficient general version of the continuous-time hybridization-expansion (CT-HYB) quantum Monte Carlo solver, which allows us to investigate ordering phenomena in strongly correlated transition-metal oxides with more realistic model Hamiltonians at experimental low temperatures. Our implementation of CT-HYB QMC works for systems of arbitrary symmetry. In cases where symmetry allows (i.e., if the local Hamiltonian does not mix flavors) we use the fast segment solver. In more realistic situations we use the Krylov approach and, away from phase transition, trace truncation. We find that in all considered cases the minus-sign problem mostly appears when off-diagonal crystal-field terms are present. It is strongly suppressed in the basis of crystal-field states, whereas off-diagonal terms of the hybridization function matrix are not as critical.[33] We show that spin-flip and pair-hopping terms hardly affect the strength of the superexchange orbital-order transition temperature in rare-earth manganites. They also do not change the conclusion for the d^1 perovskites, where orbital fluctuations are strongly suppressed by the crystal-field splitting in $YTiO_3$. For this Mott insulator we extended the calculations to very low temperatures, allowing us to observe the transition to ferromagnetism at a critical temperature $T_C \sim 50$ K, in excellent agreement with experiments. This result shows that the predicted orbital order is fully compatible with ferromagnetism. Finally we test the classical t_{2g} spin approximation for $LaMnO_3$ by comparing the results of a two-band model with the e_g electron coupled to classical (disordered) t_{2g} spins with the results for the full five-band model including all d electrons explicitly. We find that both approaches give almost the same occupied e_g orbital, while the e_g-t_{2g} spin-spin correlation function calculated from the full d model is $\sim$0.74, very close to the value expected for aligned e_g and t_{2g} spins, as assumed in the two-band model. Surprisingly, even the e_g spectral matrices resulting from the two calculations agree well. Finally we find that the t_{2g} screening included in the five-band model reduces the e_g-e_g Coulomb repulsion by about 10%.

ACKNOWLEDGMENTS

Calculations were done on the Jülich Blue Gene/Q and Juropa. We acknowledge financial support from the Deutsche Forschungsgemeinschaft through research unit FOR 1346.

APPENDIX: GENERAL CT-HYB SOLVER

In this Appendix we fix the notation and explain the details of our implementation of the general CT-HYB quantum-impurity solver. The DMFT quantum-impurity Hamiltonian is $H = H_{\rm loc} + H_{\rm bth} + H_{\rm hyb}$, where

$$H_{\rm loc} = \sum_{\alpha\bar{\alpha}} \tilde{\varepsilon}_{\alpha\bar{\alpha}} c^\dagger_\alpha c_{\bar{\alpha}} + \frac{1}{2}\sum_{\alpha\alpha'}\sum_{\bar{\alpha}\bar{\alpha}'} U_{\alpha\alpha'\bar{\alpha}\bar{\alpha}'} c^\dagger_\alpha c^\dagger_{\alpha'} c_{\bar{\alpha}'} c_{\bar{\alpha}},$$

$$H_{\rm bth} = \sum_\gamma \epsilon_\gamma b^\dagger_\gamma b_\gamma,$$

$$H_{\rm hyb} = \sum_\gamma \sum_\alpha [V_{\gamma,\alpha} c^\dagger_\alpha b_\gamma + {\rm H.c.}].$$

The combined index $\alpha = m\sigma$ labels spin and orbital degrees of freedom (flavors). For the bath, we use, without loss of generality,[35] the basis which diagonalizes $H_{\rm bth}$, with quantum numbers γ. Finally, we define $\tilde{\varepsilon}_{\alpha\bar{\alpha}} = \varepsilon_{\alpha\bar{\alpha}} - \Delta\varepsilon^{\rm DC}_{\alpha\bar{\alpha}}$, where $\varepsilon_{\alpha\bar{\alpha}}$ is the crystal-field matrix and $\Delta\varepsilon^{\rm DC}_{\alpha\bar{\alpha}}$ is the double counting correction; for the cases considered in the present paper the latter is a shift of the chemical potential μ.

1. Hybridization-function expansion

By expanding the partition function in powers of $H_{\rm hyb}$ and going to the interaction picture $H_{\rm hyb}(\tau) = e^{\tau(H_{\rm bth}+H_{\rm loc})} H_{\rm hyb} e^{-\tau(H_{\rm bth}+H_{\rm loc})}$ with $\beta = 1/k_B T$ we obtain the series

$$\begin{aligned} Z &= {\rm Tr}\left[e^{-\beta(H_{\rm bth}+H_{\rm loc})}\mathcal{T} e^{-\int_0^\beta d\tau H_{\rm hyb}(\tau)}\right] \\ &= \sum_{m=0}^{\infty}(-1)^m \int^{(m)} d\boldsymbol{\tau}\ {\rm Tr}\,\mathcal{T}\left[e^{-\beta(H_{\rm bth}+H_{\rm loc})}\prod_{i=m}^{1} H_{\rm hyb}(\tau_i)\right], \end{aligned}$$

where $\mathcal{T}$ is the time order operator, $\boldsymbol{\tau} = (\tau_1, \tau_2, \ldots, \tau_m)$ with $\tau_{i+1} \geqslant \tau_i$ and

$$\int^{(m)} d\boldsymbol{\tau} \equiv \int_0^\beta d\tau_1 \cdots \int_{\tau_{m-1}}^\beta d\tau_m.$$

In the trace only terms containing an equal number of creation and annihilation operators in both the bath and impurity sector, i.e., only even expansion orders $m = 2n$, contribute. Introducing the bath partition function $Z_{\rm bth} = {\rm Tr}\, e^{-\beta H_{\rm bth}}$, the partition function can be factorized:

$$\frac{Z}{Z_{\rm bth}} = \sum_{n=0}^{\infty}\int^{(n)} d\boldsymbol{\tau}\int^{(n)} d\bar{\boldsymbol{\tau}}\ \sum_{\boldsymbol{\alpha}\bar{\boldsymbol{\alpha}}} z^{(n)}_{\boldsymbol{\alpha},\bar{\boldsymbol{\alpha}}}(\boldsymbol{\tau},\bar{\boldsymbol{\tau}}), \qquad (2)$$

with

$$z^{(n)}_{\boldsymbol{\alpha},\bar{\boldsymbol{\alpha}}}(\boldsymbol{\tau},\bar{\boldsymbol{\tau}}) = t^{(n)}_{\boldsymbol{\alpha},\bar{\boldsymbol{\alpha}}}(\boldsymbol{\tau},\bar{\boldsymbol{\tau}})\, d^{(n)}_{\bar{\boldsymbol{\alpha}},\boldsymbol{\alpha}}(\boldsymbol{\tau},\bar{\boldsymbol{\tau}}).$$

The first factor is the trace over the impurity states

$$t^{(n)}_{\boldsymbol{\alpha},\bar{\boldsymbol{\alpha}}}(\boldsymbol{\tau},\bar{\boldsymbol{\tau}}) = {\rm Tr}\,\mathcal{T}\left[e^{-\beta(H_{\rm loc}-\mu N)}\prod_{i=n}^{1} c_{\alpha_i}(\tau_i) c^\dagger_{\bar{\alpha}_i}(\bar{\tau}_i)\right],$$

where $c^{(\dagger)}_\alpha(\tau) = e^{\tau(H_{\rm loc}-\mu N)} c^{(\dagger)}_\alpha e^{-\tau(H_{\rm loc}-\mu N)}$ and N is the total number of electrons on the impurity. For expansion order $m = 2n$, the vector $\boldsymbol{\alpha} = (\alpha_1, \alpha_2, \ldots, \alpha_n)$ gives the flavors α_i associated with the n annihilation operators on the impurity at imaginary times τ_i, while the $\bar{\boldsymbol{\alpha}} = (\bar{\alpha}_1, \bar{\alpha}_2, \ldots, \bar{\alpha}_n)$ are

associated with the n creation operators at $\bar{\tau}_i$. The second factor is the trace over the noninteracting bath, which is given by the determinant

$$d^{(n)}_{\tilde{\boldsymbol{\alpha}},\boldsymbol{\alpha}}(\boldsymbol{\tau},\bar{\boldsymbol{\tau}}) = \det\left[F^{(n)}_{\tilde{\boldsymbol{\alpha}},\boldsymbol{\alpha}}(\boldsymbol{\tau},\bar{\boldsymbol{\tau}})\right]$$

of the $n \times n$ square hybridization-function matrix with matrix elements $[F^{(n)}_{\tilde{\boldsymbol{\alpha}},\boldsymbol{\alpha}}(\boldsymbol{\tau},\bar{\boldsymbol{\tau}})]_{i',i} = F_{\tilde{\alpha}_{i'}\alpha_i}(\bar{\tau}_{i'} - \tau_i)$ given by

$$F_{\tilde{\alpha}\alpha}(\tau) = \sum_{\gamma} \frac{V_{\gamma,\tilde{\alpha}}\bar{V}_{\gamma,\alpha}}{1+e^{-\beta\epsilon_\gamma}} \times \begin{cases} -e^{-\epsilon_\gamma \tau} & \tau > 0, \\ e^{-\epsilon_\gamma(\beta+\tau)} & \tau < 0. \end{cases}$$

On the Fermionic Matsubara frequencies, ω_n, its Fourier transform

$$F_{\tilde{\alpha}\alpha}(\omega_n) = \sum_{\gamma} \frac{V_{\gamma,\tilde{\alpha}}\bar{V}_{\gamma,\alpha}}{i\omega_n - \epsilon_\gamma}$$

is related to the bath Green's function matrix $\mathcal{G}$ by

$$F_{\tilde{\alpha}\alpha}(\omega_n) = i\omega_n\delta_{\tilde{\alpha}\alpha} - \tilde{\varepsilon}_{\tilde{\alpha}\alpha} - (\mathcal{G})^{-1}_{\tilde{\alpha}\alpha}(\omega_n),$$

as can be shown by downfolding[36]

$$(\mathcal{G})^{-1}(\omega_n) = \left(\begin{array}{c|ccc} i\omega_n I_0 - H_0 & V_{1,0} & V_{2,0} & \dots \\ \hline \bar{V}_{1,0} & i\omega_n - \epsilon_1 & 0 & \dots \\ \bar{V}_{2,0} & 0 & i\omega_n - \epsilon_2 & \dots \\ \vdots & \vdots & \vdots & \ddots \end{array}\right)$$

to the impurity block ($i = 0$). Here the matrix elements of H_0 and I_0 are given by $(H_0)_{\alpha\tilde{\alpha}} = \tilde{\varepsilon}_{\alpha\tilde{\alpha}}$ and $(I_0)_{\alpha\tilde{\alpha}} = \delta_{\alpha,\tilde{\alpha}}$, while $(V_{0,i})_{\tilde{\alpha}i} = V_{\tilde{\alpha},i}$ and $(\bar{V}_{i,0})_{i\alpha} = \bar{V}_{i,\alpha}$.

To speed up the calculations, we exploit symmetries. If N_b blocks of flavors are decoupled by symmetries, the hybridization-function matrix is block diagonal in those flavors. We then write the partition function in terms of the expansion orders n_b in each block, with $n = \sum_{b=1}^{N_b} n_b$, $\boldsymbol{\tau} = \sum_{b=1}^{N_b} \boldsymbol{\tau}_b$, and $\boldsymbol{\alpha} = \sum_{b=1}^{N_b} \boldsymbol{\alpha}_b$. Thus,

$$\frac{Z}{Z_{\text{bth}}} = \left[\prod_{b=1}^{N_b}\sum_{n_b=0}^{\infty}\int^{(n_b)} d\boldsymbol{\tau}_b \int^{(n_b)} d\bar{\boldsymbol{\tau}}_b \sum_{\boldsymbol{\alpha}_b\tilde{\boldsymbol{\alpha}}_b}\right] z^{(n)}_{\boldsymbol{\alpha},\tilde{\boldsymbol{\alpha}}}(\boldsymbol{\tau},\bar{\boldsymbol{\tau}})$$

with

$$d^{(n)}_{\tilde{\boldsymbol{\alpha}},\boldsymbol{\alpha}}(\boldsymbol{\tau},\bar{\boldsymbol{\tau}}) = \prod_{b=1}^{N_b} d^{(n_b)}_{\tilde{\boldsymbol{\alpha}}_b,\boldsymbol{\alpha}_b}(\boldsymbol{\tau}_b,\bar{\boldsymbol{\tau}}_b)$$

and

$$t^{(n)}_{\boldsymbol{\alpha},\tilde{\boldsymbol{\alpha}}}(\boldsymbol{\tau},\bar{\boldsymbol{\tau}}) = \text{Tr}\,\mathcal{T}\left[e^{-\beta(H_{\text{loc}}-\mu N)}\prod_{b=1}^{N_b}\prod_{i=n_b}^{1} c_{\alpha_{bi}}(\tau_{bi})c^{\dagger}_{\tilde{\alpha}_{bi}}(\bar{\tau}_{bi})\right].$$

2. Segment solver and Krylov approach

Calculating the trace over the impurity states involves propagating states in the impurity Hilbert space. For models with many orbitals this can become very demanding. We therefore use a multi-approach scheme. When the on-site Hamiltonian conserves the flavors we use the so-called segment approach,[8] which is extremely fast. In such cases only terms with an equal number of creation and annihilation operators *per flavor* contribute to the local trace, and it is convenient to express the partition function in expansion orders n_a for flavors a. The partition function then can be rewritten as

$$\frac{Z}{Z_{\text{bth}}} = \left[\prod_{a=1}^{N_a}\sum_{n_a=0}^{\infty}\int^{(n_a)} d\boldsymbol{\tau}_a \int^{(n_a)} d\bar{\boldsymbol{\tau}}_a\right] z^{(n)}_{\boldsymbol{\alpha},\tilde{\boldsymbol{\alpha}}}(\boldsymbol{\tau},\bar{\boldsymbol{\tau}}).$$

Here $\boldsymbol{\tau} = \sum_{a=1}^{N_a} \boldsymbol{\tau}_a$ and $\bar{\boldsymbol{\tau}} = \sum_{a=1}^{N_a} \bar{\boldsymbol{\tau}}_a$, while the vectors $\boldsymbol{\alpha} = \sum_{a=1}^{N_a} \boldsymbol{\alpha}_a$ and $\tilde{\boldsymbol{\alpha}} = \sum_{a=1}^{N_a} \tilde{\boldsymbol{\alpha}}_a$ have the n_a components $\alpha_{ai} = \tilde{\alpha}_{ai} = a$. The local trace factors into

$$t^{(n)}_{\boldsymbol{\alpha},\tilde{\boldsymbol{\alpha}}}(\boldsymbol{\tau},\bar{\boldsymbol{\tau}}) = \text{Tr}\,\mathcal{T}\left[e^{-\beta(H_{\text{loc}}-\mu N)}\prod_{a=1}^{N_a}\prod_{i=n_a}^{1} c_a(\tau_{ai})c^{\dagger}_a(\bar{\tau}_{ai})\right]$$
$$= \left(\prod_{a=1}^{N_a} s_a^{n_a}\right) e^{-\sum_{aa'}[(\tilde{\varepsilon}_{aa}-\mu)\delta_{a,a'}+\frac{1}{2}\tilde{u}_{aa'}]l_{aa'}},$$

where $l_{aa'}$ is the length of the overlap of the τ segments a and a', $s_a = \text{sgn}(\tau_{a1} - \bar{\tau}_{a1})$ is the Fermionic sign, and $\tilde{u}_{aa'} = U_{aa'a'a} + U_{aa'aa'}$ is the interaction.

In all the cases in which the local Hamiltonian mixes flavors, we adopt the Krylov method.[11] At the beginning of the DMFT loop we calculate all the eigenstates of H_{loc}, $\{|\Psi_n\rangle\}$, and their energies $\{E_n\}$; a given state $|\Psi_n\rangle$ is then propagated with $e^{-\tau_1 E_n}$. The first creation or annihilation operator met generates a new state $|\Psi\rangle$, which we propagate with $e^{-(\tau_2-\tau_1)H_{\text{loc}}}$ obtaining $|\Psi(\tau_2-\tau_1)\rangle$, and we repeat the procedure until the last creation or annihilation operator is met. At the core of the procedure are the matrix-vector multiplications and the propagation of vectors. For the first aspect, we work in the occupation number basis, in which H_{loc} and the creation and annihilation operators are sparse matrices. Additionally, we arrange the states according to the symmetries[10,12] of H_{loc}, so that we have sparse block-diagonal matrices and can exploit to the maximum efficient sparse-matrix multiplication algorithms. We find that this typically reduces the CPU time by, e.g., about 15% for a three-band model. We use the Krylov approach to calculate $|\Psi(\tau)\rangle = e^{-H_{\text{loc}}\tau}|\Psi\rangle$. First we construct the Krylov space of order r, $\mathcal{K}_r(|\Psi\rangle)$, i.e., the space spanned by $|\Psi\rangle, H_{\text{loc}}|\Psi\rangle, H^2_{\text{loc}}|\Psi\rangle, \dots, H^r_{\text{loc}}|\Psi\rangle$. By means of the Lanczos[36] technique we construct an orthonormal basis for $\mathcal{K}_r(|\Psi\rangle)$, $\{|k\rangle\}$; in this basis H_{loc} is tridiagonal with eigenstates $\{|l\rangle\}$ and energies $\{\varepsilon_l\}$. The matrix exponential $e^{-H_{\text{loc}}\tau}$ is approximated by its projection onto the Krylov space, $e^{-H_{\text{loc}}\tau}|\Psi\rangle \sim |\Psi(\tau)\rangle_r = \sum_{l=0}^{r} e^{-\tau\varepsilon_l}|l\rangle\langle l|\Psi\rangle$. This procedure converges very rapidly with r, typically for r much smaller than the dimension of the Hilbert space,[37,38] as illustrated in Fig. 4. We find that the convergence slightly deteriorates with increasing τ and the complexity of the Hamiltonian (realistic Coulomb vertex, crystal-field matrix), but typically two to three steps are sufficient to obtain accurate results. To best exploit the power of the method, we keep r flexible. Furthermore, to avoid that the norm of the state becomes very large during the propagation, we set E_0 to zero, i.e., substitute $e^{-\tau H_{\text{loc}}}$ with $e^{-\tau(H_{\text{loc}}-E_0)}$. In addition, the procedure (propagation and creation/annihilation) is carried out from both the left and the right sides of the trace to minimize the work needed to measure, e.g., the Green's function matrix. Finally, at low temperatures or far from phase transitions we use the eigenvalues of H_{loc} to determine the relevant energy

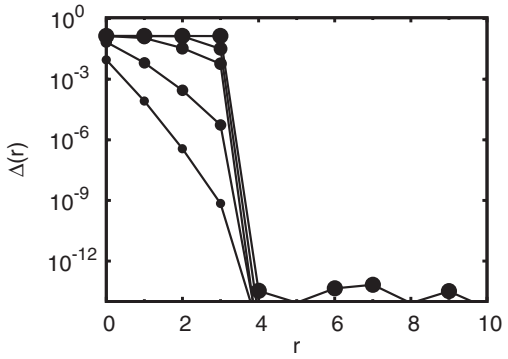

FIG. 4. Convergence of the Krylov approximation $|\psi(\tau)\rangle_r$ to $|\psi(\tau)\rangle = e^{-(H_{\rm loc}-E_0)\tau}|\psi\rangle$ for a representative test case (five-orbital model, half filling). The figure shows the difference $\Delta(r) = ||\psi(\tau)\rangle_r - |\psi(\tau)\rangle|$. Symbols (in order of increasing size) represent $\tau = 0.005$, 0.05, 0.5, 5, and 100.

window and truncate adaptively the outer bracket of the trace. This further reduces the CPU time.

The performance of our CT-HYB QMC solver (Krylov and segment version) on the Jülich BlueGene/Q, and comparison with Hirsch-Fye QMC, is shown in Fig. 5.

3. Green's function and occupation matrix

The partition function (2) can be seen as the sum over all configurations $c = \{\alpha_i \tau_i, \bar{\alpha}_i \bar{\tau}_i, n\}$ in imaginary time and flavors. In a compact form,

$$Z = \sum_c \langle Z \rangle_c = \sum_c w_c \sim \sum_{\{c\}} \mathrm{sign}(w_c),$$

where in the last term the sum is over a sequence of configurations $\{c\}$ sampled by the Monte Carlo approach using $|w_c|$ as the probability of configuration c. In the segment solver approach, we parametrize the configurations by intervals $[0,\beta)$ (time line), occupied by a sequence of creators and annihilators, which define segments on the time line. The basic Monte Carlo updates are addition and removal of segments, antisegments, or complete lines.[8] In the Krylov solver approach we use the insertion and removal of pairs of creation and annihilation operators[9,10] as basic updates. In addition, we shift operators in time[8,10] and exchange the configurations of blocks or flavors[39] (global moves). Finally, a generic observable O can then be obtained as a Monte Carlo average:

$$O \sim \frac{\sum_{\{c\}} \langle O \rangle_c \ \mathrm{sign}(w_c)}{\sum_{\{c\}} \mathrm{sign}(w_c)},$$

where $\langle O \rangle_c$ is the value of the observable for configuration c, and c runs over the configurations visited with probability $|w_c|$ during the sampling. The average expansion order increases linearly with the inverse temperature. For the case of $YTiO_3$, at ∼40 K, the average expansion order is $n \sim 40$.

We calculate the Green's function matrix in two ways, directly[8,12] and via Legendre polynomials.[40] In the first approach, the Green's function matrix is obtained as a Monte Carlo average with $\langle O \rangle_c = \langle G_{\alpha\bar{\alpha}} \rangle_c$, and

$$\langle G_{\alpha\bar{\alpha}} \rangle_c = \sum_{b=1}^{N_b} \sum_{i,j=1}^{n_b} \Delta(\tau, \tau_{bj} - \bar{\tau}_{bi}) [M^{(n_b)}]_{bj,bi} \delta_{\alpha_{bj}\alpha} \delta_{\bar{\alpha}_{bi}\bar{\alpha}}.$$

Here $M^{(n)} = [F^{(n)}]^{-1}$ is the inverse of the hybridization-function matrix, which we update at each accepted move, while Δ is given by

$$\Delta(\tau,\tau') = -\frac{1}{\beta} \begin{cases} \delta(\tau - \tau') & \tau' > 0, \\ -\delta(\tau - (\tau' + \beta)) & \tau' < 0, \end{cases}$$

and the δ function is discretized. In the second approach, we calculate the Legendre coefficients $\langle O \rangle_c = \langle G^l_{\alpha\bar{\alpha}} \rangle_c$, with

$$\langle G^l_{\alpha\bar{\alpha}} \rangle_c = \sum_{b=1}^{N_b} \sum_{i,j=1}^{n_b} P_l(\tau_{bj} - \bar{\tau}_{bi}) [M^{(n_b)}]_{bj,bi} \delta_{\alpha_{bj}\alpha} \delta_{\bar{\alpha}_{bi}\bar{\alpha}},$$

$$P_l(\tau) = -\frac{\sqrt{2l+1}}{\beta} \begin{cases} p_l(x(\tau)), & \tau > 0, \\ -p_l(x(\tau + \beta)), & \tau < 0, \end{cases}$$

where $p_l(x)$ is a Legendre polynomial of rank l, with $x(\tau) = 2\tau/\beta - 1$, and we reconstruct the Green's function matrix from

$$G_{\alpha\bar{\alpha}}(\tau) = \sum_{l=0}^{\infty} \frac{\sqrt{2l+1}}{\beta} p_l(x(\tau)) G^l_{\alpha\bar{\alpha}}.$$

Concerning occupations, in the segment solver we calculate them from the total length of the segments of the different flavors;[8] in the Krylov solver we obtain them in two ways, directly from the Green's function and by explicitly inserting the occupation number operator at the center of the operator sequence ($\tau = \beta/2$) and calculating the corresponding trace.[9,11] The off-diagonal elements of the local occupation matrix $\langle c^\dagger_\alpha c_{\bar{\alpha}} \rangle$, which cannot be obtained by inserting the corresponding operators at $\tau = \beta/2$,[41] are extracted from the Green's function matrix only.

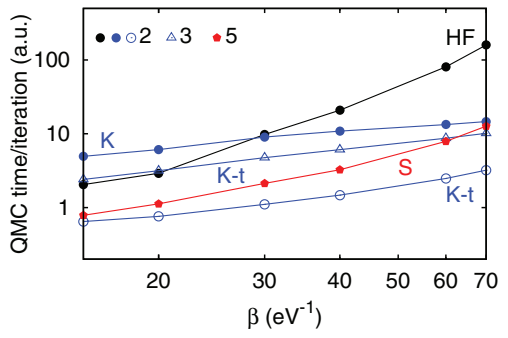

FIG. 5. (Color online) Scaling of our CT-HYB QMC LDA + DMFT code on BlueGene/Q. Black line: Hirsch-Fye (HF) solver, two orbitals. The dark and light lines are CT-HYB calculations. Dark lines: Krylov solver with truncation of the local trace (open symbols, K-t) and without (solid symbols, K). Results are for two (circles) and three (triangles) orbitals. Light lines: Segment solver (S), five-band model (pentagons). All points correspond to calculations of high quality (and with comparable error bars) for the systems considered in this work. For $\beta = 70$ (∼165 K) the five-orbital segment solver is about as fast the three-orbital Krylov with trace truncation or the two-orbital Krylov without trace truncation, and it is remarkably faster than the two-orbital HF solver.

[1] V. I. Anisimov, A. I. Poteryaev, M. A. Korotin, A. O. Anokhin, and G. Kotliar, J. Phys.: Condens. Matter **9**, 7359 (1997); A. I. Lichtenstein and M. I. Katsnelson, Phys. Rev. B **57**, 6884 (1998).

[2] E. Pavarini, E. Koch, D. Vollhardt, and A. Lichtenstein (eds.), *The LDA + DMFT Approach to Strongly Correlated Materials*, Modeling and Simulation, Vol. 1 (Verlag der Forschungszentrum Jülich, 2011).

[3] See, e.g., E. Pavarini in Ref. 2.

[4] A. Georges, G. Kotliar, W. Krauth, and M. J. Rozenberg, Rev. Mod. Phys. **68**, 13 (1996).

[5] E. Pavarini and E. Koch, Phys. Rev. Lett. **104**, 086402 (2010).

[6] E. Pavarini, S. Biermann, A. Poteryaev, A. I. Lichtenstein, A. Georges, and O. K. Andersen, Phys. Rev. Lett. **92**, 176403 (2004).

[7] E. Pavarini, E. Koch, and A. I. Lichtenstein, Phys. Rev. Lett. **101**, 266405 (2008).

[8] P. Werner, A. Comanac, L. de Medici, M. Troyer, and A. J. Millis, Phys. Rev. Lett. **97**, 076405 (2006).

[9] P. Werner and A. J. Millis, Phys. Rev. B **74**, 155107 (2006).

[10] K. Haule, Phys. Rev. B **75**, 155113 (2007).

[11] A. M. Läuchli and P. Werner, Phys. Rev. B **80**, 235117 (2009).

[12] E. Gull, A. J. Millis, A. I. Lichtenstein, A. N. Rubtsov, M. Troyer, and P. Werner, Rev. Mod. Phys. **83**, 349 (2011).

[13] For a pedagogical introduction, see P. Werner in Ref. 2.

[14] B. Surer, M. Troyer, P. Werner, T. O. Wehling, A. M. Läuchli, A. Wilhelm, and A. I. Lichtenstein, Phys. Rev. B **85**, 085114 (2012).

[15] C. Ulrich, G. Khaliullin, S. Okamoto, M. Reehuis, A. Ivanov, H. He, Y. Taguchi, Y. Tokura, and B. Keimer, Phys. Rev. Lett. **89**, 167202 (2002).

[16] E. Pavarini, A. Yamasaki, J. Nuss, and O. K. Andersen, New J. Phys. **7**, 188 (2005).

[17] G. Zhang, E. Gorelov, E. Koch, and E. Pavarini, Phys. Rev. B **86**, 184413 (2012).

[18] J. Rodríguez-Carvajal, M. Hennion, F. Moussa, A. H. Moudden, L. Pinsard, and A. Revcolevschi, Phys. Rev. B **57**, R3189 (1998); J.-S. Zhou and J. B. Goodenough, *ibid.* **68**, 144406 (2003); Phys. Rev. Lett **96**, 247202 (2006).

[19] A. Flesch, G. Zhang, E. Koch, and E. Pavarini, Phys. Rev. B **85**, 035124 (2012).

[20] L. F. Feiner and A. M. Oles, Phys. Rev. B **59**, 3295 (1999); in this early model study, the authors estimate T_{KK} for $LaMnO_3$ as large as 500 K.

[21] O. Gunnarsson, E. Koch, and R. M. Martin, Phys. Rev. B **54**, R11026 (1996).

[22] M. De Raychaudhury, E. Pavarini, and O. K. Andersen, Phys. Rev. Lett. **99**, 126402 (2007).

[23] E. Gorelov, M. Karolak, T. O. Wehling, F. Lechermann, A. I. Lichtenstein, and E. Pavarini, Phys. Rev. Lett. **104**, 226401 (2010).

[24] K. I. Kugel and D. I. Khomskii, Zh. Eksp. Teor. Fiz. **64**, 1429 (1973) [Sov. Phys. JEPT **37**, 725 (1973)].

[25] K. H. Ahn and A. J. Millis, Phys. Rev. B **61**, 13545 (2000).

[26] A. Yamasaki, M. Feldbacher, Y.-F. Yang, O. K. Andersen, and K. Held, Phys. Rev. Lett. **96**, 166401 (2006).

[27] T. Mizokawa and A. Fujimori, Phys. Rev. B **54**, 5368 (1996).

[28] B. Keimer, D. Casa, A. Ivanov, J. W. Lynn, M. V. Zimmermann, J. P. Hill, D. Gibbs, Y. Taguchi, and Y. Tokura, Phys. Rev. Lett. **85**, 3946 (2000); G. Khaliullin, Phys. Rev. B **64**, 212405 (2001).

[29] G. Khaliullin and S. Okamoto, Phys. Rev. Lett. **89**, 167201 (2002); Phys. Rev. B **68**, 205109 (2003).

[30] M. Cwik, T. Lorenz, J. Baier, R. Muller, G. Andre, F. Bouree, F. Lichtenberg, A. Freimuth, R. Schmitz, E. Muller-Hartmann, and M. Braden, Phys. Rev. B **68**, 060401 (2003).

[31] J. P. Goral and J. E. GreedanJ. Magn. Magn. Mater. **37**, 315 (1983).

[32] J. P. Goral, J. E. Greedan, and D. A. MacLean, J. Solid State Chem. **43**, 244 (1982).

[33] For the cases in which the hybridization function is diagonal in the flavors, and the local Hamiltonian does not mix flavors, there is no sign problem. To see this, we observe that the sign of the local trace is $\prod_{a=1}^{N_a} s_a^{n_a}$, as shown in the Appendix, Sec. 2. The determinant of the hybridization-function matrix factorizes in the product $d^{(n)}_{\tilde{\boldsymbol{\alpha}},\boldsymbol{\alpha}}(\boldsymbol{\tau},\bar{\boldsymbol{\tau}}) = \prod_{a=1}^{N_a} d^{(n_a)}_{\tilde{\boldsymbol{\alpha}}_a,\boldsymbol{\alpha}_a}(\boldsymbol{\tau}_a,\bar{\boldsymbol{\tau}}_a)$. We then factor out the Fermionic sign $s_a^{n_a}$ of each $d^{(n_a)}_{\tilde{\boldsymbol{\alpha}}_a,\boldsymbol{\alpha}_a}(\boldsymbol{\tau}_a,\bar{\boldsymbol{\tau}}_a)$; the remaining term $s_a^{n_a} d^{(n_a)}_{\tilde{\boldsymbol{\alpha}}_a,\boldsymbol{\alpha}_a}(\boldsymbol{\tau}_a,\bar{\boldsymbol{\tau}}_a)$ is positive, as can be shown by transforming the bath Hamiltonian for flavor a into a one-dimensional chain, as done in Ref. 34 for the Anderson model and the Hirsch-Fye algorithm.

[34] J. Yoo, S. Chandrasekharan, R. K. Kaul, D. Ullmo, and H. U. Baranger, J. Phy. A: Math. Gen. **38**, 10307 (2005).

[35] E. Koch, G. Sangiovanni, and O. Gunnarsson, Phys. Rev. B **78**, 115102 (2008).

[36] See, e.g., E. Koch in Ref. 2.

[37] J. Jaklič and P. Prelovšek, Phys. Rev. B **49**, 5065 (1994).

[38] M. Hochbruck and C. Lubich, SIAM J. Numer. Anal. **34**, 1911 (1997).

[39] A. I. Poteryaev, M. Ferrero, A. Georges, and O. Parcollet, Phys. Rev. B **78**, 045115 (2008).

[40] L. Boehnke, H. Hafermann, M. Ferrero, F. Lechermann, and O. Parcollet, Phys. Rev. B **84**, 075145 (2011).

[41] For observables that cannot be expressed as expectation values of density operators, measuring by insertion at $\beta/2$ is not necessarily ergodic. This is particularly apparent for, e.g., $\langle c^\dagger_\alpha(\tau) c_{\bar{\alpha}}(\tau)\rangle$ with $\alpha \neq \bar{\alpha}$; if the off-diagonal crystal-field matrix elements are zero, by inserting $c^\dagger_\alpha(\beta/2) c_{\bar{\alpha}}(\beta/2)$ in the local trace we obtain $\langle c^\dagger_\alpha(\tau) c_{\bar{\alpha}}(\tau)\rangle = 0$, even if the hybridization-function matrix is not diagonal.